Journal of Coastal Research	14	1	315–330	Royal Palm Beach, Florida	Winter 1998

Measuring and Modelling Sediment Transport on a Macrotidal Ridge and Runnel Beach: An Intercomparison

G. Voulgaris†⁺, D. Simmonds‡, D. Michel††, H. Howa††, M.B. Collins† and D.A. Huntley‡

† Department of Oceanography
University of Southampton
Southampton Oceanography Centre
European Way
Southampton SO14 3ZH, UK

†† Département de Géologie et Océanographie
URA CNRS 197
Université Bordeaux I
Avenue des Faultés
33405 Talence Cedex, France

‡ Institute of Marine Studies
University of Plymouth
Drake Circus
Plymouth PL4 8AA, UK

ABSTRACT

VOULGARIS, G.; SIMMONDS, D.; MICHEL, D.; HOWA, H.; COLLINS, M.B., and HUNTLEY, D.A., 1998. Measuring and modelling sediment transport on a macrotidal ridge and runnel beach: An intercomparison. *Journal of Coastal Research,* 14(1), 315–330. Royal Palm Beach (Florida), ISSN 0749-0208.

Observations of hydrodynamics, fluorescent tracer dispersal and beach morphology were acquired in the intertidal zone of a macrotidal ridge and runnel beach. High frequency hydrodynamic data from pressure transducers and electromagnetic current meters were used to describe flow patterns in the intertidal zone while sediment transport rates were estimated using energetics and empirical models. Results from fluorescent tracer experiments provided information on net sediment movement over periods ranging from one to five tidal cycles whereas morphometric analysis was carried out to determine net beach movement during a period of 24 tidal cycles.

Comparison of the results showed that sediment transport based on the hydrodynamic measurements did not agree with sediment movement derived using the tracer and morphometric methods. This disagreement is because the latter methods integrate processes occurring throughout the whole tidal cycle including those at very low water depths (swash zone processes). Hydrodynamic data were limited to periods of the tidal cycle where the mean water depth was greater than 0.5 m. Such limitation, imposed by the physical dimensions, principle of operation and installation procedures of the instruments is common in nearshore studies. Sediment transport results obtained by using hydrodynamic data obtained in macrotidal areas would be incomplete if swash-zone processes are not covered by the sampling scheme. However, comparison of results obtained for shorter periods (*i.e.* excluding shallow water) with those from other methods that integrate over the whole tidal cycle can be used to extract information on sedimentary processes for periods where no direct data are available.

ADDITIONAL INDEX WORDS: *Sediment transport measurements, hydrodynamics, intertidal zone, macrotidal beach, ridge and runnel beach, tracer, waves, currents, sediment transport modelling.*

INTRODUCTION

Net convergence and/or divergence of sediment transport, over a tidal cycle, controls the formation and maintenance of ridge, runnels and any other morphological forms present in the nearshore zone. These types of formations have been described qualitatively in terms of beach response to calm and storm events (WRIGHT and SHORT, 1984; HAYES, 1972; OWENS and FROBEL, 1977; HINE, 1979; MULRENNAN, 1992; SIMMONDS *et al.*, 1995). Such an approach is descriptive presently and has not been formulated into an accurate quantitative prediction of beach change. This is due to the complex combination of motions and the number of scales involved in sediment movement.

HORIKAWA (1981) has classified the coastal processes according to the time- and space-scales involved into *macroscale*, *mesoscale* and *microscale*. The former takes place over time-scales that vary from a few years to hundreds of years whereas the morphological features associated with them can extend over hundreds of metres to kilometres (*i.e.*, formation of spits, tidal inlets, cliffs *etc.*). These processes are traditionally studied by geologists and geomorphologists. Mesoscale processes operate within hours or days and the space scales involved extend from a few meters to hundreds of meters (*i.e.*, beach cusps, bars, *etc.*). Finally, turbulence and wave dynamics are typical examples of microscale processes occurring within seconds or fractions of a second and at space-scales extending from millimeters (*i.e.*, turbulence) to a few metres (*i.e.*, wave-induced oscillations). In theory, the superimposition of microscale phenomena should constitute mesoscale phenomena and those of mesoscale, likewise, the macroscale phenomena.

96064 received 20 June 1996; accepted in revision 14 October 1996.

⁺ Present address: Woods Hole Oceanographic Institution, Woods Hole, MA 02543, USA.

The present study was funded by the Commission of the European Community (Directorate General for Science, Research and Development) under Contract No. MAS2-CT92-0024-C (C-STAB).

Woods Hole Oceanographic Institution Contribution No: 9259.

Traditionally, sediment transport studies were focused on either macroscale or mesoscale processes. The development of fast-response instrumentation for the measurement of currents (electromagnetic current meter, HUNTLEY and BOWEN, 1975) and suspended sediment concentrations (optical backscatter sensors, DOWNING *et al.*, 1981; acoustic backscatter sensors, VINCENT *et al.*, 1991) enabled the study of sediment transport processes at the microscale. Using these type of sensors, JAFFE *et al.* (1984) showed that sediment transport rates based on mean offshore flow (averaged over 30 min) did not agree with the onshore migration of a sub-tidal bar (averaged over a period of 6.5 hours). Examination of the instantaneous fluxes revealed that sediment transport occurring at time-scales associated to individual wave periods (a few seconds) was responsible for an onshore flux of sediment in suspension that controlled the bar movement. Factors such as the asymmetry of shoaling waves and the phase difference between oscillatory flow and the maximum suspended sediment concentration appear to have an important influence on the sediment transport.

These findings regarding the role of microscale processes in the development of local morphology, combined with the advancement of the appropriate technology for measurements of the instantaneous hydrodynamic conditions established a new trend in studying coastal processes. High frequency sensors constituted of an integral part of the standard instrumentation for every major nearshore field or laboratory experimental study carried out over the past decade (*i.e.*, DUCK85, MASON *et al.*, 1988; NSTS, GUZA and THORNTON, 1989; C^2S^2, BOWEN *et al.*, 1986; SUPERDUCK, ROSATI *et al.*, 1990; DELILAH, SCOTT *et al.*, 1991; B-BAND, DAVIDSON *et al.*, 1992; SUPERTANK, KRAUS and SMITH, 1994). In parallel, the use of these sensors provides information on the asymetry of the flow field in the nearshore (GUZA and THORNTON, 1985). The technological advances in flow measurements were accompanied with the development of sophisticated sediment transport models (BAILARD, 1981) which account for the asymmetric character of the waves and the different periods of oscillation present in the nearshore (FOOTE and HUNTLEY, 1994). Such models are widely used for the prediction of sediment movement and morphodynamic modelling (ROELVICK and STIVE, 1989; SCOTT *et al.*, 1991).

Although, high frequency measurements are very important in studying the processes involved in sediment resuspension and transport mechanisms, the validity of the results is limited to conditions similar to those during the data collection period. Extrapolation of these point measurements for morphological modelling requires stationarity of the driving mechanism (*i.e.*, hydrodynamics). Such stationarity can be found at non-tidal environments or at areas where the mean water depth is large in relation to the tidal range (*i.e.*, inner continental shelf). It does not apply, though to areas where the mean water depth varies significantly during the tidal cycle (*i.e.*, intertidal zone). There the processes vary within a tidal cycle from shoaling wave (CONLEY and INMAN, 1992), breaking and bore-like waves (NIELSEN, 1984; STERNBERG *et al.*, 1989) to inner-surf and swash-zone processes (BEACH and STERNBERG, 1988). The contibution of each of these processes is different for various locations within the intertidal zone. MASSELINK (1993), modelling the effect of tidal inundation in hydrodynamic processes, showed that swash-zone processes dominate the high tidal zone, while the mid-tidal zone is dominated by shoaling-wave processes.

The present study illustrates this difficulty in extracting definitive information on sediment transport and morphological development in macrotidal environments from high frequency measurements alone. An investigation, in parallel, of various time-scales of coastal processes is needed to understand the complete sediment transport mechanisms and the contribution of a particular scale of process to the next. Observations of hydrodynamics and sediment movement, collected during various time- and space-scales are presented. Shoaling and outer surf zone hydrodynamic measurements were carried out using rapid sampling measurement stations. Time-series of instantaneous velocity (microscale) were used to estimate sediment transport rates by the application of empirical formulae and models. Tidally-averaged sediment transport patterns were obtained from fluorescent tracer experiments, whereas information on beach morphology on longer time-scale (several days) was obtained through the analysis of topographic data. The results obtained from the different approaches have been integrated in order to identify the dominant sedimentary processes. This approach has revealed the complexity of the sedimentary processes and highlighted the difficulty in using high-frequency data for the extraction of information on the development of beach morphology in particular in areas with large tidal range (macrotidal).

EXPERIMENTAL SITE & PROCEDURES

Field measurements were obtained at Nieuwpoort-aan-Zee, situated some 13 km southwest of Oostende (Figure 1(a)), from 20th February–4th March 1994 (Julian days 51–63). The experimental site was outside the influence of man-made obstructions, such as groynes, which are common along this coast. The sediment was well sorted, fine/medium sand (mean grain size 0.183 mm); at the time of the observations the average beach slope ($\tan\beta$) was 0.012 with an intertidal zone of between 250 and 500 m wide. The experimental site exhibited typical ridge and runnel beach characteristics (Figure 1c) with up to five well-defined ridges exposed at low tide.

Tides in this area are semi-diurnal with a large neap-to-spring variation of between 2.7 to 6.5 m during the deployment period (Figure 2). Tidal currents in the inner shelf are characterised by elongate and asymmetrical tidal current ellipses, with a northeasterly-directed residual flood displacement controlling the sub-tidal sediment transport pathways (DE MOOR, 1991).

The wave climate of the area is typical of short-fetched seas with wave periods 3 to 6 sec (Figure 3). However, typical wave periods recorded during the deployment were between 4 and 12 seconds with offshore wave heights on the order of 0.5 to 1 m. Dominant wave direction offshore as extracted from wave hindcasting modelling (U.K. MET Office, Figure 3c), is primarily from the west–southwest (23% of the time) and secondarily from the north–northeast (10% of the time).

Time-series of flow velocities, tide and wave-induced pres-

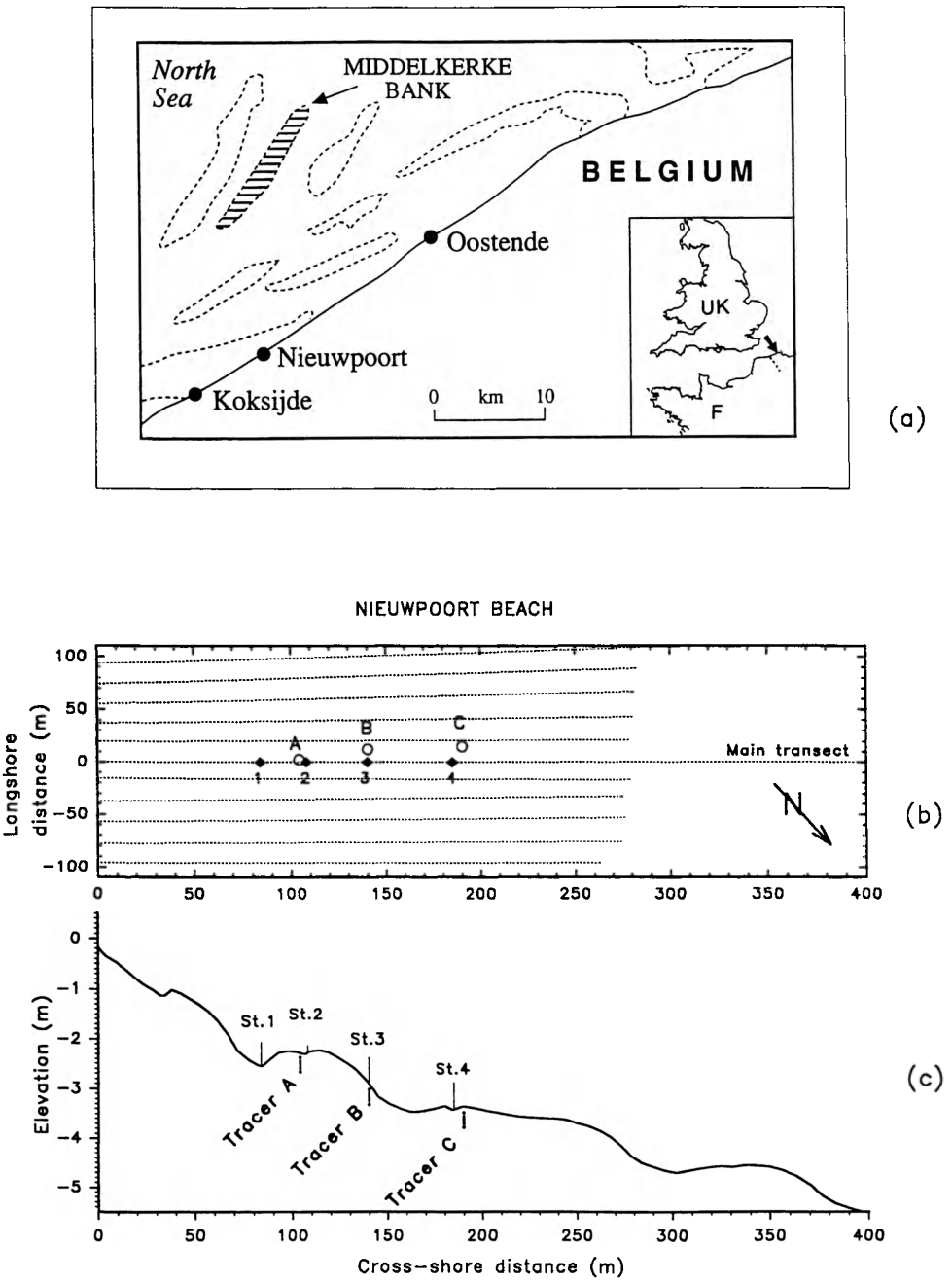

Figure 1. (a) Location map of the study area. Plan-view (b), and cross-sectional profile (c) of the intertidal zone of the experimental site. Locations of instrument stations (St. 1, 2, 3 and 4) and sand tracer injection points (tracer A, B and C) are shown on (b) and (c), respectively. Dashed lines on (b) indicate locations of topographic survey transects.

sure and suspended sediment concentrations were measured at four locations in the high and mid-tidal zones (Figure 1). The instruments consisted of electromagnetic current meters (Stations 1, 2, 3 and 4), pressure transducers (Stations 2, 3 and 4) and optical backscatter (OBS) sensors which measured suspended sediment concentration at various elevations above the sea bed. Twenty (20) minutes of burst data were collected simultaneously at all stations. The sampling frequency within each burst was either 4 or 8 Hz. More detailed information on the experimental procedure can be found elsewhere (SIMMONDS *et al.*, 1995). Hydrodynamic data collected at Station 3 are presented in this study. The instrument suite of this station consisted of 3 electromagnetic current meters installed at 16, 42 and 101 cm above the bed, one pressure transducer located at 20 cm above the seabed and 6 OBS sensors installed at 10, 17, 30.5, 42, 53.5 and 101.5 cm above

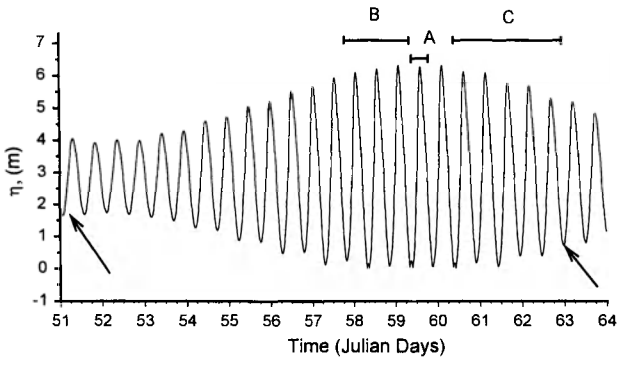

Figure 2. Predicted (ADMIRALTY TIDE TABLE, 1994) tidal elevations at Oostende during the study period. Horizontal bars indicate time and duration of tracer experiments.

the seabed. For the period of the tracer experiments the OBS sensors failed to operate. In addition, the sea water quality was such (*i.e.* high concentration of algae) that an estimate of suspended sediment transport using OBS data would have been of limited value. Data only from the lower electromagnetic current meter and the pressure transducer are presented here.

Fluorescent tracer was used to study tidally-averaged sediment transport rates at the field site. The tracer consisting of natural sand from the study area which was dyed in the laboratory using acrylic fluorescent paint. The tracer sand, released during each of these experiments, was deposited in a 1 m × 1 m × 0.05 m pit, during low water, then covered with 0.5 cm of natural sand, and the dispersion was monitored during subsequent low water periods. An automated counter (HOWA and DE RESSEGUIER, 1994) was used to detect tracer concentration at surficial sampling locations on a grid with 2 m × 2 m mesh size, over an area extending approximately 90 m alongshore and 30 m in the shore-normal direction. Detection was complemented with the collection of cores from the tracer dispersion area. The cores also were used to estimate the thickness of the mobile (transport) layer.

Three different tracer experiments (A, B and C) were carried out over the intertidal zone at the experimental site (Figures 1 and 2; Table 1). Detection of the moving tracer is denoted in the illustrations by a tracer letter, with a subscript referring to the measurement sequence (*e.g.*, B_2 refers to results obtained from tracer experiment B, during the 2nd survey/detection).

During tracer experiment A, 50 kg of green dyed sand was injected and searched for only once, during the following low tide (A_1). This particular (green) colour tracer was later abandoned, due to the presence of shell debris having the same fluorescent characteristics. Fourty (40) kg of red tracer were injected during experiment B, with detection undertaken during the subsequent three low tides (B_1, B_2 and B_3). Fifty (50) kg of red tracer were used for tracer experiment C, with detection during 5 low tides (C_1 to C_5).

The orthogonal system used for presenting the hydrodynamic and tracer data is defined as the x-axis being in the cross-shore direction (positive onshore) and the y-axis aligned in the longshore direction (positive towards the Netherlands *i.e.* northeast).

Additionally, topographic data were collected at low water during daylight hours, throughout the experimental period (Julian days 51–63). The data consisted of a detailed beach profile along the (main) transect of the hydrodynamic stations (Figure 1c) and 10 additional profiles parallel to the main transect, at approximately 20 m intervals (shown as dotted lines on Figure 1b). Due to the limited time available for surveying the intertidal zone, the spatial resolution along the latter profiles was less detailed than along the main transect. An electronic theodolite integrated with an Electronic Distance Measurement (EDM) instrument was used for the topographic survey. The EDM and theodolite instrumental errors were ± 0.3 cm and ± 0.0014 degs, respectively. Typical errors for the survey data presented here was calculated to be smaller than 0.4 cm and 1 cm for horizontal and vertical distances.

METHODOLOGY AND DATA ANALYSIS

Modelling Sediment Transport

Various empirical sediment transport formulae, applied to the marine environment were developed initially for fluvial or aeolian studies (*e.g.* MEYER-PETER and MULLER, 1948; EINSTEIN, 1972; YALIN 1977). Most of these formulae are power laws relating the sediment transport rate to the excess velocity or shear stress:

$$Q = k\cdot(u - u_{cr})^b \text{ or } k'\cdot(\tau_b - \tau_{cr})^{b'} \qquad (1)$$

where u and τ_b are the flow velocity and bottom shear stress, u_{cr} and τ_{cr} are the critical velocity or bottom shear stress required for the initiation of sediment movement and k and k′ are empirical coefficients expressing the efficiency of the flow in moving the sediments of the sea bed.

In the marine environment, under the combined action of waves and currents, the response of the sea bed to oscillatory flow is rapid (MADSEN, 1991). To account for oscillatory waves, instantaneous values of shear stress (τ_{wc}) used in the sediment transport formulae are integrated over a complete wave cycle. The relationship used in this analysis is a modification of the MEYER-PETER and MULLER (1948) formula, resembling equation (1) (shear stress version) with a power index of b′ = 3/2. To indicate relative sediment transport intensity and direction, the quantity $(\tau_{wc} - \tau_{cr})^{3/2}$ is referred to as the *sediment transport index* (STI). The instantaneous index was calculated for each hydrodynamic data burst measured during the tracer experiments and for 2 cases: (i) under the wave crest and (ii) under the wave trough.

Application of this empirical model requires the prediction of bottom shear stress from various hydrodynamic parameters. With a knowledge of the sensor heights and the mean water depth (h), the significant wave height (H_{sig}) and amplitudes of horizontal current oscillations (u, v) were derived from the variance of each depth corrected time-series using the following approximate relationships:

$$H_{sig} = 4\cdot\sigma_h, \qquad U_b = 2\cdot\sigma_u, \qquad V_b = 2\cdot\sigma_v \qquad (2)$$

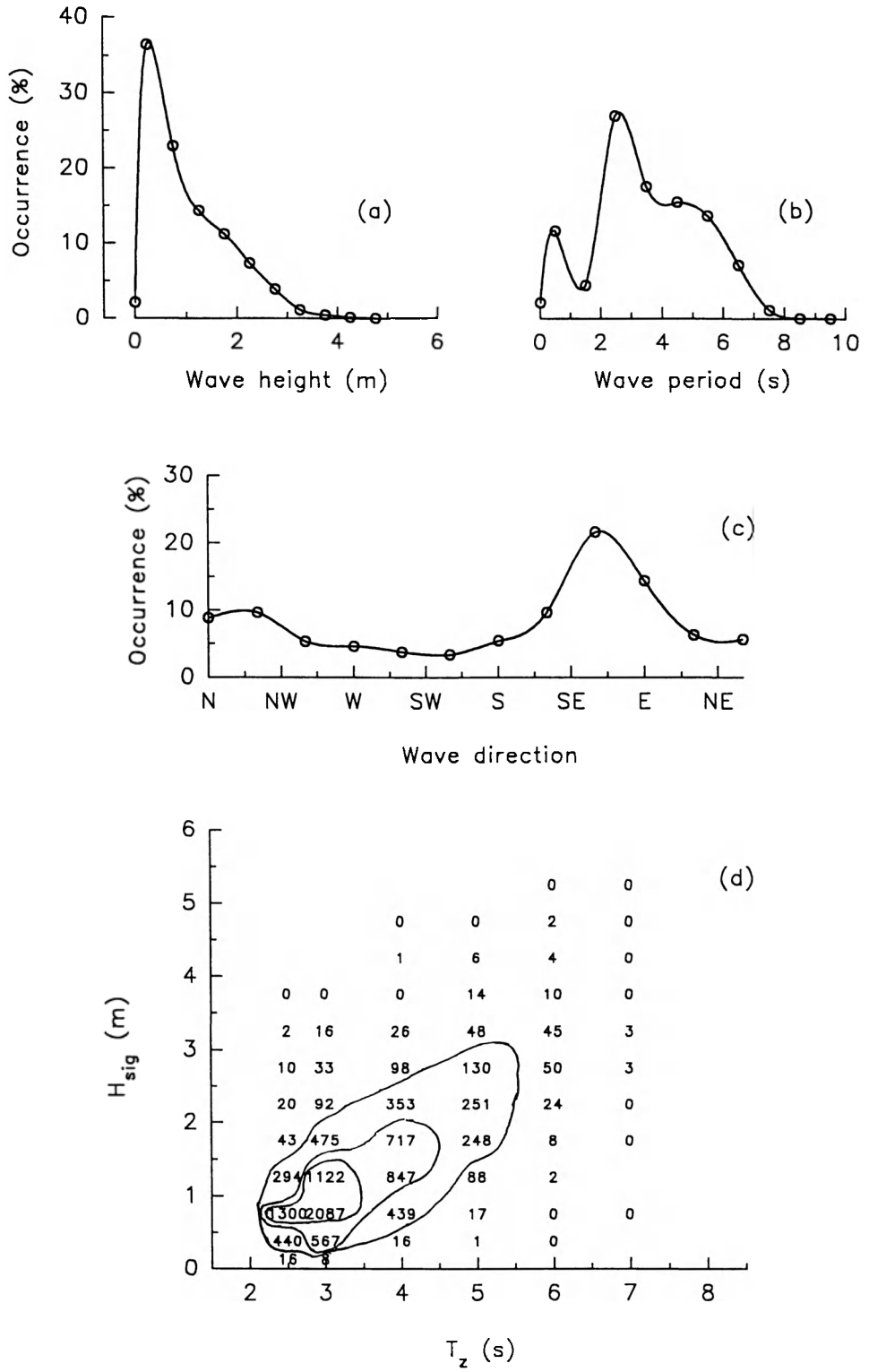

Figure 3. Offshore wave climate for the experimental area. Predicted wave climate from wind data: percentage of occurrence of (a) significant wave height; (b) wave periods and (c) direction of wave approach. (d) Joint distribution of wave height and zero-up-crossing periods measured offshore the experimental area during the period Oct. 1977–Dec. 1986.

Table 1. *Tracer experiment data and results.*

Tracer Experiment	Date/Time of Detection	Detection	Duration of Submersion (s)	Centroid Coordinates (m) Absolute Y	Absolute X	Relative Yi	Relative Xi	Distance D (m)	Tracer Thickness Zt (m)	Depth of Disturbance Zo (m)
A	059/10:00									
	059/19:00	A_1	5670	0.73	1.42	0.73	1.42	1.56	0.015	0.025
B	057/19:00									
	058/08:00	B_1	16480	−3.07	2.23	−3.07	2.23	3.79	0	0.04
	058/18:30	B_2	16832	4.23	4.71	7.3	2.53	7.73	0	0.028
	059/08:30	B_3	16714	−1.05	7.04	−5.28	2.33	5.77	0	0.022
C	060/10:00									
	060/20:00	C_1	20524	0.36	1.76	0.36	1.76	1.8	0.025	0.025
	061/11:00	C_2	20926	0.08	3.6	−0.28	1.84	1.86	0.025	0.03
	061/21:00	C_3	20524	3.04	5.64	2.96	2.04	3.59	0.02	0.025
	062/11:30	C_4	20618	2.27	4.98	−0.77	−0.66	1.03	0.017	0.02
	062/21:30	C_5	20457	4.51	4.79	2.24	−0.19	2.7	0.015	0.035

Tracer Experiment	Date/Time of detection	Centroid Velocity (m/s × 10^{-6}) Vy	Vx	IVI	Q (m^3/s per m width × 10^{-6}) Qy	Qx	IQI	Recovery Rate %
A	059/10:00	129	250	275	1.94	3.75	4.12	11
	059/19:00							
B	057/19:00	−186	135	230	−4.47	3.25	5.53	80
	058/08:00	434	150	459	7.29	2.53	7.71	75
	058/18:30	−316	139	345	−4.17	1.84	4.56	72
	059/08:30							
C	060/10:00	18	86	88	0.26	1.29	1.32	30
	060/20:00	−13	88	89	−0.24	1.58	1.60	30
	061/11:00	144	99	175	2.16	1.49	2.63	50
	061/21:00	−37	32	50	−0.45	−0.38	0.60	31
	062/11:30	109	9	132	2.29	−0.20	2.77	24
	062/21:30							

where σ_h, σ_u and σ_v are the standard deviations about the mean of h, u and v, respectively. The peak wave period was also estimated from spectral analysis of the horizontal current time-series. In addition, burst-averaged mean ($\langle u \rangle$, $\langle v \rangle$), root mean squared values (U_{rms}, V_{rms}) and the angles of approach of both waves and the steady currents were calculated using the time-series of the horizontal components of the flow.

This information was used to drive a parameterised version of FREDSOE's (1984) wave-current interaction model (SOULSBY *et al.*, 1993). The model was used to estimate bottom shear stress, τ_c due to mean currents in the presence of waves and the maximum wave-induced shear stress, τ_w. The maximum *total* wave-current shear stress τ_{wc} is then defined as the vector sum of these quantities. The model was applied assuming the presence of a planar sea bed (skin friction only). The model results are presented in terms of two pairs of horizontal components, τ_{wcx} (cross-shore), and τ_{wcy} (longshore), beneath both a wave crest and through:

$$\tau_{wcx} = |\tau_c| \cdot \cos(\phi_c) \pm |\tau_w| \cdot \cos(\phi_w)$$
$$\tau_{wcy} = |\tau_c| \cdot \sin(\phi_c) \pm |\tau_w| \cdot \sin(\phi_w) \quad (3)$$

where ϕ_c and ϕ_w are the anticlockwise measured angles of the tidal current and wave propagation vectors to the shore-normal. The positive sign in eqn. (3) is used for calculating the combined shear stress beneath the wave crest whereas the negative sign is used for the calculation of the shear stress beneath the wave trough.

MADSEN and GRANT's (1976) modified Shields diagram was used for deriving the critical shear stress for naturally occurring beach sands (0.16 N/m^2).

Besides the sediment transport index (STI) model, BAILARD's (1981) energetics-based model predictions were compared to the tracer experiment results. This model combines transport components induced by wave-asymmetry and mean flow (on the basis of BAGNOLD's (1963) energetics approach); it is used most widely in morphological model approaches (*e.g.* ROELVICK and STIVE, 1989; SCOTT *et al.*, 1991) and is considered one of the best theoretical models for time-dependent, cross-shore sediment transport (SCHOONES and THERON, 1995).

The expression for the total (*i.e.*, bedload and suspended load, I_t) time-averaged immersed weight sediment transport (BAILARD, 1981) is:

$$\langle I_t \rangle = \rho \cdot C_f \cdot \frac{\epsilon_B}{\tan \phi} \cdot \left[\langle |\mathbf{u}^2 \mathbf{u}| \rangle + \frac{\tan \beta}{\tan \phi} \cdot \langle |\mathbf{u}|^3 \rangle \mathbf{i} \right] + \rho \cdot C_f \cdot \frac{\epsilon_s}{W} \cdot \left[\langle |\mathbf{u}|^3 \mathbf{u} \rangle + \frac{\epsilon_s}{W} \cdot \tan \beta \langle |\mathbf{u}|^5 \rangle \mathbf{i} \right] \quad (4)$$

where the settling velocity (W) of the sands was calculated to be 0.22 cm/sec, ϵ_b and ϵ_s are the bedload and suspended load

efficiency factors taken as 0.2 and 0.025, after GUZA and THORNTON (1985). C_f is a drag coefficient assumed as 0.005 after BOWEN (1980) and ϕ is the particle internal friction angle. The unit vector **i** is directed down-slope in the offshore (−x) direction, whereas **u** is the vector of the total instantaneous velocity measured at the nearest instrument station. The local mean bed slopes, $tan\beta$, were calculated for the beach profile data and they were 0.0081, 0.032 and 0.001 for tracer locations A, B and C.

Decomposition of eqn (4) into the two horizontal components, as presented by GUZA and THORNTON (1985), enables the prediction of longshore and cross-shore immersed weight sediment transport rates using the measured longshore and cross-shore components of the flow.

Sediment Transport Rates, Based upon the Tracer Experiments

Monitoring dyed sand movement to determine *in-situ* beach sand transport has been used since the 1950's (INMAN and CHAMBERLAIN, 1959). Such an approach requires two basic assumptions. First, the dyed sand behaves in the same manner as the natural sand and, second, the tracer movement can be monitored accurately. The first assumption is fulfilled if the labelling procedure does not alter the physical and hydrodynamic properties of the sediment. The second assumption can be assessed by evaluating the percentage recovery rate of marked material during the tracing experiment.

The sand is assumed to move as a uniform layer of thickness Z_o at a velocity **U**. The immersed weight sediment transport rate (I) is then given by the relationship:

$$I = (\rho_s - \rho)\cdot g\cdot Q = (\rho_s - \rho)\cdot g\cdot c_b\cdot U\cdot Z_o \qquad (5)$$

where Q is the volumetric sediment transport rate, ρ_s and ρ are the sand particle and sea water densities, respectively, and g is acceleration due to gravity. c_b is the volume concentration of the sand within the bed (0.50–0.65). A volume concention of 0.60 suggested by WHITE (1987) has been used in this study. The transport velocity (**U**) is determined on the basis of movement of the mass centroid of the tracer, divided by the time of submergence between detections (WHITE, 1987).

The recovery rate was defined for each survey as the percentage ratio of the mass of detected tracer outside the release point, M_D, and the difference between the total amount of released tracer, M_R and the mass of tracer, M_{Di} remaining at the release point.

$$\text{Recovery Rate (\%)} = \frac{100\cdot M_D}{M_R - M_{Di}}. \qquad (6)$$

RESULTS

Tidal Inundation and Morphological Interpretation

The topography of this macrotidal beach reveals a number of different morphological regimes which must be considered in relation to tidal excursion. The intertidal zone exposed during spring tides has an average slope of 0.012 and can be subdivided into three zones between spring high water level (SHWL), neap high water level (NHWL), neap low water level (NLWL) and spring low water level (SLWL). These are referred to as high (SHWL–NHWL), mid- (NHWL–NLWL) and low (SLWL–NLWL) tidal zones (WRIGHT *et al.*, 1982) and are shown in Figure 4a. Each of these zones is characterised by morphological regimes which respond differently to hydrodynamics and timescales of inundations (MASSELINK, 1993). The fraction of time (p) of a complete tidal cycle, during which any particular location on the profile is inundated, was calculated (WRIGHT *et al.*, 1982) for typical spring (solid line), neap (dotted line) and mean (dashed line) tides (see Figure 4).

The high tidal zone is inundated for about 20% of time during spring tide and 10% for a mean tide. The mid-tidal zone is, on average, inundated for 60% of the time throughout all tidal cycles. In comparison, the low tidal zone is inundated almost 100% of the time during neap and mean tides and approximately 90% of the time during spring tides.

Longshore uniformity at the experimental site was confined to distances of approximately 500 m and was interrupted by drainage channels. However, the cross-sectional profile is typical of this region of coastline (Figure 4a). Five ridges, with associated runnels were identified along the intertidal zone. The most inshore berm-like ridge was situated within the middle of the high tidal zone. The next ridge offshore (Figure 1c) was the site for tracer experiments A and B. This ridge which is approximately 35cm high, is located at the boundary between high and mid-tidal zones, coincident with neap high water level. Hydrodynamic data collected from the seaward side of this ridge are presented in this study (Station 3, see Figures 1c and 4a). A large ridge, almost 140 m wide and with an average height of 20 cm, is found at the mid-tidal zone and at mean water level. At the boundary between the mid- and low-tidal zones, there is another ridge of some 25 cm high. A similar feature also is found within the low tidal zone; it does not exceed 20 cm in height.

Hydrodynamic Interpretation

Pressure and current data recorded at station 3, over the three tide periods are presented in this section. Data collection at the high frequency measuring stations is limited to the time during which the sensors were fully immersed *i.e.* for burst-averaged water depths $h > 0.80$ m (minimum depth 0.5 m) at station 3. In view of the low wave energy during this deployment ($H_{sig} < 0.20$m), this water depth typifies shoaling waves conditions, *i.e.*, conditions outside the surf zone. Some of the measured parameters are shown in Figure 5.

Longshore currents during the experiment were tidally driven. The flows which were recorded over the upper half of the intertidal zone are directed mainly towards the northeast (the Netherlands) attaining their maximum magnitude of around 30 cm/sec at the beginning of the flood. As the tide rises, the currents reduce in magnitude and reverse near low water. Although offshore the current is in phase with sea surface (tidal) elevation (*i.e.* a progressive tidal wave, LACKNEUS *et al.*, 1994), preliminary analysis of the beach data indicates that this behavior is due to bed friction which causes the longshore currents to lead the tidal elevation inshore.

During the three tides, the mean cross-shore currents var-

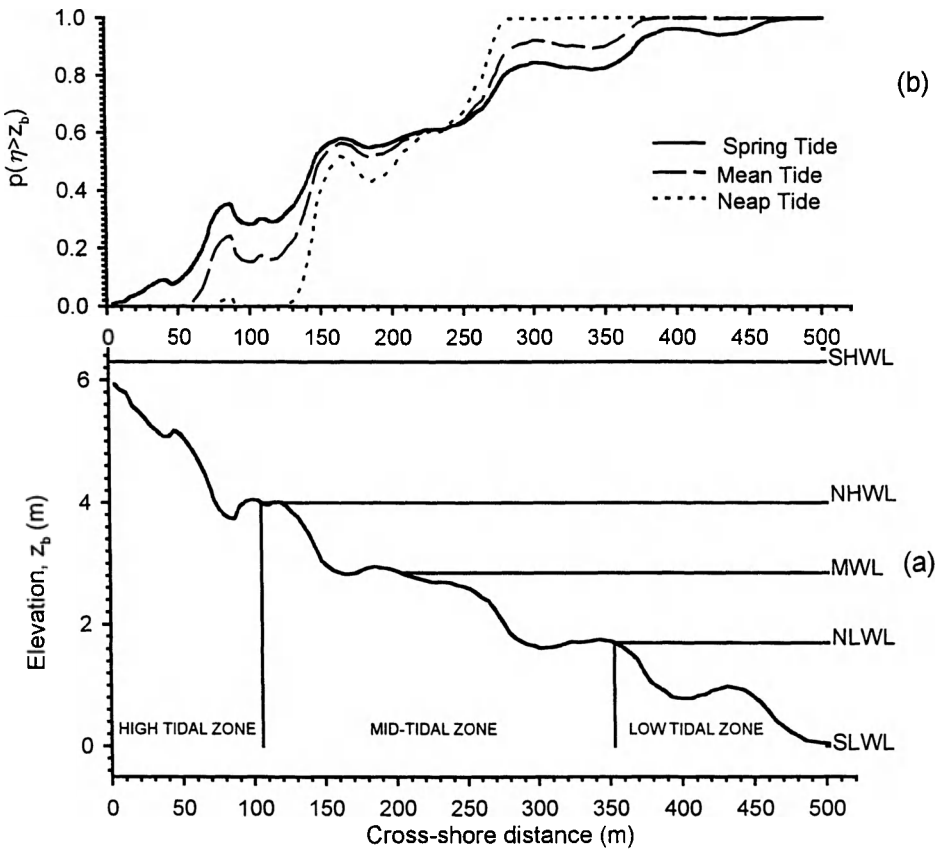

Figure 4. (a) Cross-sectional profile of the intertidal zone along the central transect (see Figure 1(b)); High, low and mean water levels for spring and neap tides are shown (for explanation see text) together with definitions of intertidal zones. (b) Relative frequency (p) of inundation over the profile for spring (solid line), neap (dotted line) and mean tides (dashed line).

ied from near zero during flood, to almost 10 cm/sec on ebb. The observed flow is caused by a combination of a steady mean offshore, hereafter referred to as "undertow," and a tidally-varying current.

In an attempt to separate the undertow from the tidal currents, a linear regression analysis was applied to the measured mean cross-shore current and the rate of change of local water depth for both the ebb and flood (Figure 6). Assuming that the cross-shore component of the mean current is due to an onshore-offshore migration of the water volume driven by the tidal flooding and ebbing over the beach topography, then the mean velocity at high water ($dh/dt = 0$) should be zero. However, the data show that a steady current over all three tides of around 5 cm/sec is present. This can be seen from the intersection of the ebb and flood regression lines (Figure 6). This value represents the average value of the undertow and its persistence at high water confirms that it is not directly related to the tidal wave.

Tidal currents oppose the undertow during the flood, so that the cross-shore mean velocity tends towards zero. During the ebb, both cross-shore current components act in the same direction, enhancing the measured offshore flow which reached up to 10 cm/sec (5 cm/sec due to undertow and 5 cm/sec due to tidal currents).

Wave-orbital velocities appear to be tidally-modulated: higher orbital velocities are observed during the ebb, than during the flood. From the ratio of the variance of the instantaneous current velocity in the alongshore and cross-shore directions, the angle of wave approach was estimated to be around 345° to shore normal incidence *i.e.* towards the northeast. From pattern of mean flows during the tidal cycle, it may be concluded that waves and currents will act in the same direction during the flood but that they oppose each other during the ebb. This results in higher orbital velocities during the ebb, as shown on Figure 5.

Tidal modulation of both the waves and currents results in variation in the dominant forces (waves or currents) throughout the tidal cycle. The ratio of maximum orbital velocity to tidal current magnitude ('wave strength') is plotted on Figure 6d against the local gradient in tidal amplitude. On average, waves dominate during the ebb while during the flood, the mean currents are of similar strength to the oscillatory current amplitudes.

Sediment Transport Model Comparison

The wave-current interaction model results are presented here with Baillards energetics model results. The purpose of

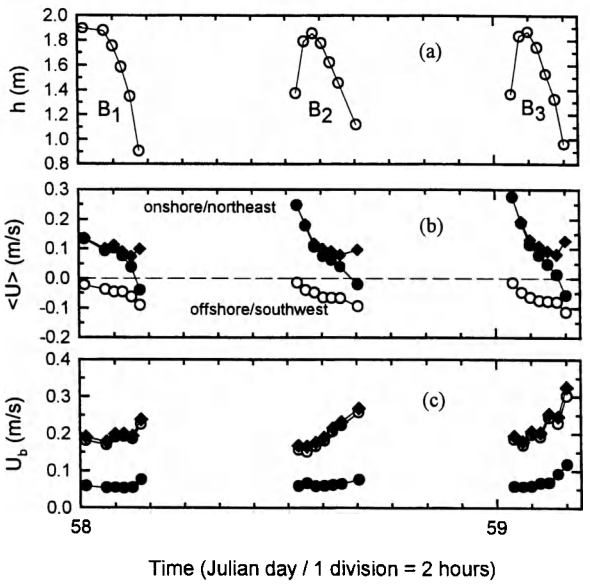

Figure 5. Hydrodynamic data collected near the tracer injection point B (instrument Station 3): (a) local mean water depth; (b) mean currents (longshore, cross-shore and total magnitude) at 16 cm above the bed; (c) significant orbital velocities (longshore, cross-shore and total). (**Key**: open circles: cross-shore currents; solid circles: longshore currents; solid diamonds: total magnitude of current).

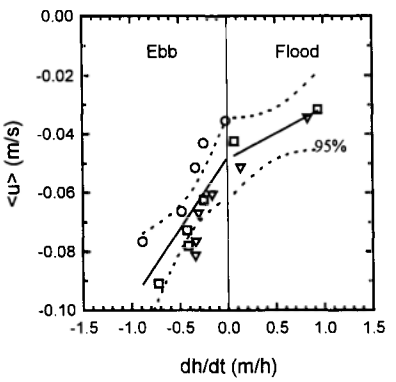

Figure 6. Measured cross-shore component of mean current (⟨u⟩) against local sea water elevation gradient (dh/dt). The results of regression analysis (solid lines) and 95% confidence intervals (dotted lines) are shown for the data obtained during the ebb and flood, respectively. (**Key**: circle, triangle and square symbols represent data from tidal cycles B_1, B_2 and B_3, respectively).

this comparison is to assess the conclusions that can be drawn with regards to the movement of sediment from hydrodynamic measurements alone made under the particular conditions experienced over the ridge and runnel field. These results will be compared later with the overall transport measured by the tracer experiment.

Wave-Current Interaction, Deterministic Modelling

Combined shear stress estimates due to combined currents and waves for cross-shore (τ_{wcx}) and longshore (τ_{wcy}) components are plotted in Figure 7. Estimates under wave crests and troughs (open and solid circles, respectively) are shown in Figures 7b and c and the total shear stresses are shown on Figure 7d. The calculated stresses are much larger than the threshold limits derived from the modified Shields diagram (MADSEN and GRANT, 1976) implying that a continuous state of sediment movement persisted throughout the tidal cycle.

The cross-shore component of the maximum wave-current bottom shear stress under the wave crest is directed onshore during flood. Under a wave trough, the forces acting on the sea bed are always directed offshore. Alongshore, the maximum combined shear stress is dominated by the mean component; thus, stresses under a wave crest and trough (Figure 7c) exhibit similar trends and magnitudes.

In contrast to the asymmetry found in the wave-induced orbital velocities (Figure 5) throughout a tidal cycle, the shear stresses (although modulated by the tides) exhibit relative symmetry around high water. Higher stresses are predicted during the first phase of the flood and last phase of the ebb tide.

The results of the wave-current interaction model have been used for the calculation of the STI (refer Methodology section) for each burst during the tidal cycle—under both a wave crest and a wave trough. The results for longshore and cross-shore directions are presented in Figure 8. The cross-

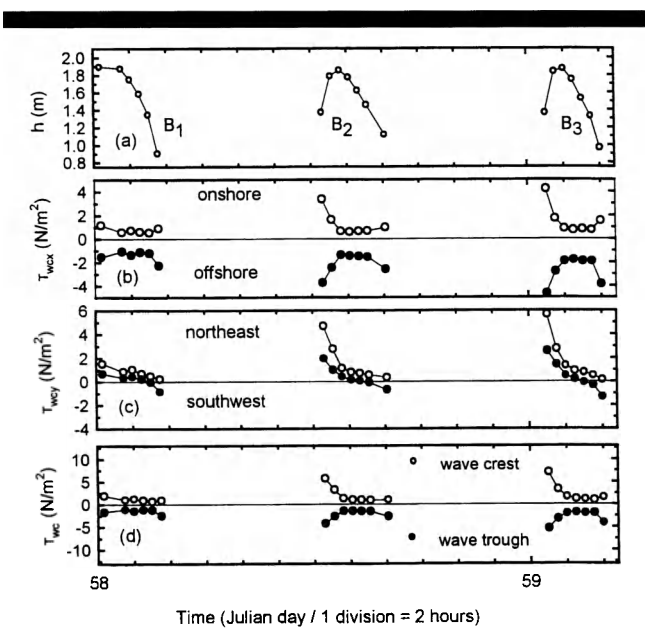

Figure 7. (a) Local mean water depth over the tracer B experiment period. Combined wave and current bottom shear stresses as predicted from the hydrodynamic measurement applying the wave current interaction model (see text). Open and solid circles indicate shear stresses under the wave crest and trough respectively: (b) cross-shore component; (c) longshore component; (d) total combined bottom shear stress (Note: Negative values are used on (c) to represent stress under wave trough). Critical shear stress for sediment motion is shown as straight lines.

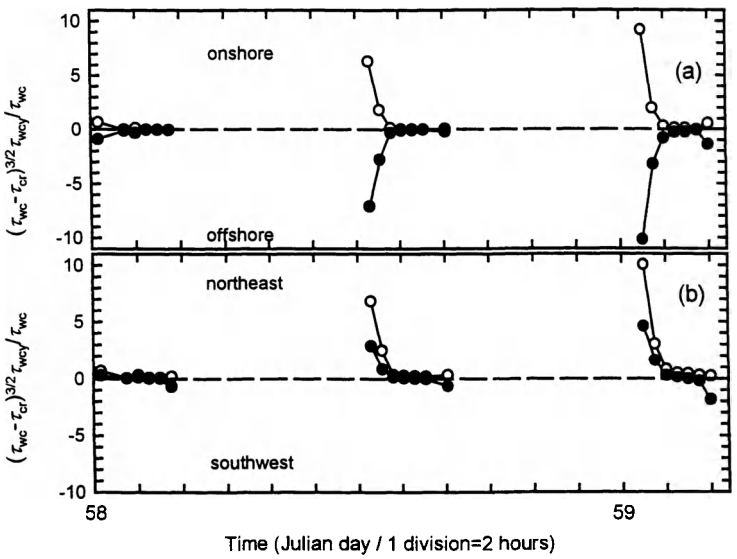

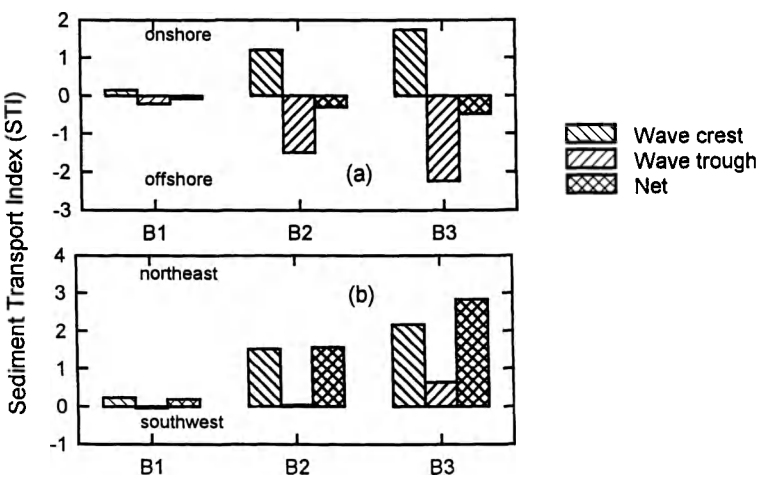

Figure 8. **Top**: Sand Transport Indices (STI) beneath a wave crest (open circles) and a wave trough (solid circles) in the alongshore (a) and cross-shore (b) directions respectively. **Bottom**: Average value of STI for the tracer B experiment period, along the cross-shore (a) and longshore (b) directions for wave crests, troughs and their vector sum (net), respectively.

shore component of the STI is greatest during the flood tide, suggesting onshore transport occurs under a wave crest and offshore transport under a trough. Alongshore, enhanced transport is predicted at the beginning of the tidal cycle in the direction of the mean current with a reversal at the end of the ebb flow. Time-averaged forms of the sediment transport indices over the measurement period suggest onshore movement occurs under a wave crest and offshore under a trough with the latter as the dominant process. Alongshore, the time-averaged STI is 0.20, 1.57 and 2.82 for the cycles B_1, B_2 and B_3 respectively, suggesting transport towards the northeast.

Energetics Approach

Bailard's model has been applied to the data set, using the electromagnetic current meter measurements again from Station 3. Results from this model, for both the cross-shore and longshore directions, are shown on Figure 9.

Decomposition of eqn (4) allows an evaluation of the relative importance of bedload, suspended load, oscillatory and mean current components. Analysis of these data revealed that: (i) the suspended load dominates the overall sediment transport processes; (ii) in the cross-shore direction, sand transport associated with wave asymmetry is much less important than that in response to the mean, offshore directed transport; (iii) similarly, mean currents dominate transport in the longshore direction, towards the northeast. The latter is concordant with the regional pattern of offshore sediment movement measured by De Moor (1991).

The importance of the mean currents as the main sediment carriers was confirmed by comparing the output of Bailard's model with sediment fluxes estimated using instantaneous

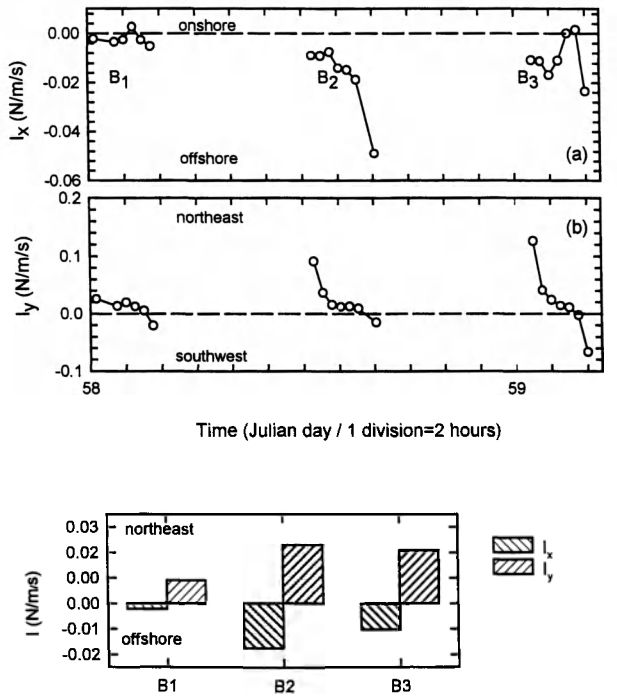

Figure 9. **Top**: Immersed weight sediment transport rate estimated over the tracer B experiment period, using Bailard's model in the shore-normal (a) and alongshore (b) directions. **Bottom**: Tidal cycle averaged sediment transport rates for both shore-normal (lx) and alongshore (ly) directions.

current velocities and suspended sediment concentration measurements from Station 4 (VOULGARIS, 1996; VOULGARIS and COLLINS, 1996).

Looking at the model results, for individual bursts, the longshore transport is seen to be directed toward the northeast during the beginning of the flood but, as the tide advances, the magnitude of the longshore sand transport rate reduces and is eventually reversed towards the end of the ebb. Cross-shore transport direction varies during the B_1 and B_3 tidal cycles but throughout tide B_2 it is directed consistently offshore.

Tidally-averaged transport rates are shown in the lower part of Figure 9; this indicates consistent offshore transport towards the northeast.

The variation, during the tidal cycle, of the STI (Figure 8) and the sediment trasport rates estimated by the Bailard's model (Figure 9) are in a qualitative agreement both in the cross-shore and longshore directions. The cross-shore component of the STI is greater during the wave trough so that a wave-averaged value STI would be in the same direction as the wave trough STI (solid circles in Figure 8a). Both STI and Bailard's model indicate that greater amounts of sediment are trasported at the beginning of the flood and the end of the ebb period, with the former being significantly larger than the latter. It is noteworthy, that those periods of high sediment mobility coinside with time of shallow water depths (see Figure 5a).

Tracer Analysis

The tracing experiment A took place at the outer region of the high tidal zone (Figures 1 and 4) in a water depth of 1.45 m at spring high water, and with wave heights of around 0.20 m and periods of 8 sec. Unfortunately the tracer recovery rate was low (11%), due to difficulties in separating the tracer from natural shell fragments with similar fluorescence. Although this tracer was followed during a single tidal cycle, the centroid can be seen to have moved in a predominantly onshore direction towards the northeast (Figure 11).

During experiment B, the tracer was released on the upper mid-tidal zone, near the lower limit of the high tidal zone. The tracer was followed over three consecutive tidal cycles, from 27/2/1994 to 28/2/1994, with a recovery rate of 72–80%. During this experiment, the local water depth varied from approximately 1.8 m to exposure at low tide. The local significant wave height measured at high water was approximately 0.15 m with wave approach consistently from the west with a wave period between 9 sec and 10 sec.

During the first tidal cycle after injection (B_1), the tracer dispersed west-east with the centroid moving south of the release point (Figure 10). This dispersion pattern is in a general agreement with the incoming wave direction. During the second tidal cycle (B_2) the tracer dispersed alongshore towards the northeast. Similar dispersion is observed for the third tidal cycle, although there is some alignment similar to that of B_1 (Figure 10). This latter pattern suggests dispersion in response to both waves and tidally-induced longshore currents.

In all the data sets, the cross-shore movement of the tracer centroid was consistently shoreward, though movement in the longshore direction being more variable. During release B, the tracer centroid initially moved in a southwesterly direction, whereas during the second detection period (B_2), the tracer moved in an opposing longshore direction (northeast); this direction was again reversed during the last tidal cycle (B_3). The cross-shore components of the sediment transport rates, derived on the basis of tracer movement, were 5.24, 4.08 and 2.97 ($\times 10^{-2}$ kg/m/sec^2) for the detection periods B_1, B_2 and B_3, respectively. The longshore components were an order of magnitude greater than the cross-shore (-7.22, 11.7 and -6.73×10^{-2} kg/m/sec^2 respectively) although of variable direction (note the sign).

The final tracer was released on the central ridge in the tidal zone. Despite significantly lower recovery rates ($X < 50\%$), the tracer was successfully measured during 5 tidal cycles. A net onshore movement during the first 2 tidal cycles can clearly be seen followed by movement toward the northeast (the Netherlands) (Figure 11). The low recovery rate is due to a rapid onshore movement of the tracer towards the runnel (Figure 1b) from where it was rapidly transported alongshore, outside the area of detection. High flow rates were observed in the runnels during the initial and final stages of the inundation as the water flowed into or out through the narrow drainage channels that breach the seaward ridge.

Morphometric Analysis

Analysis of successive beach profiles recorded along the main transect throughout the tracer experiment showed little change. Elevation changes were comparable to the experimental (survey) errors ($\pm$ 1 cm). To identify trends in beach movement, profiles taken along the main transect at the be-

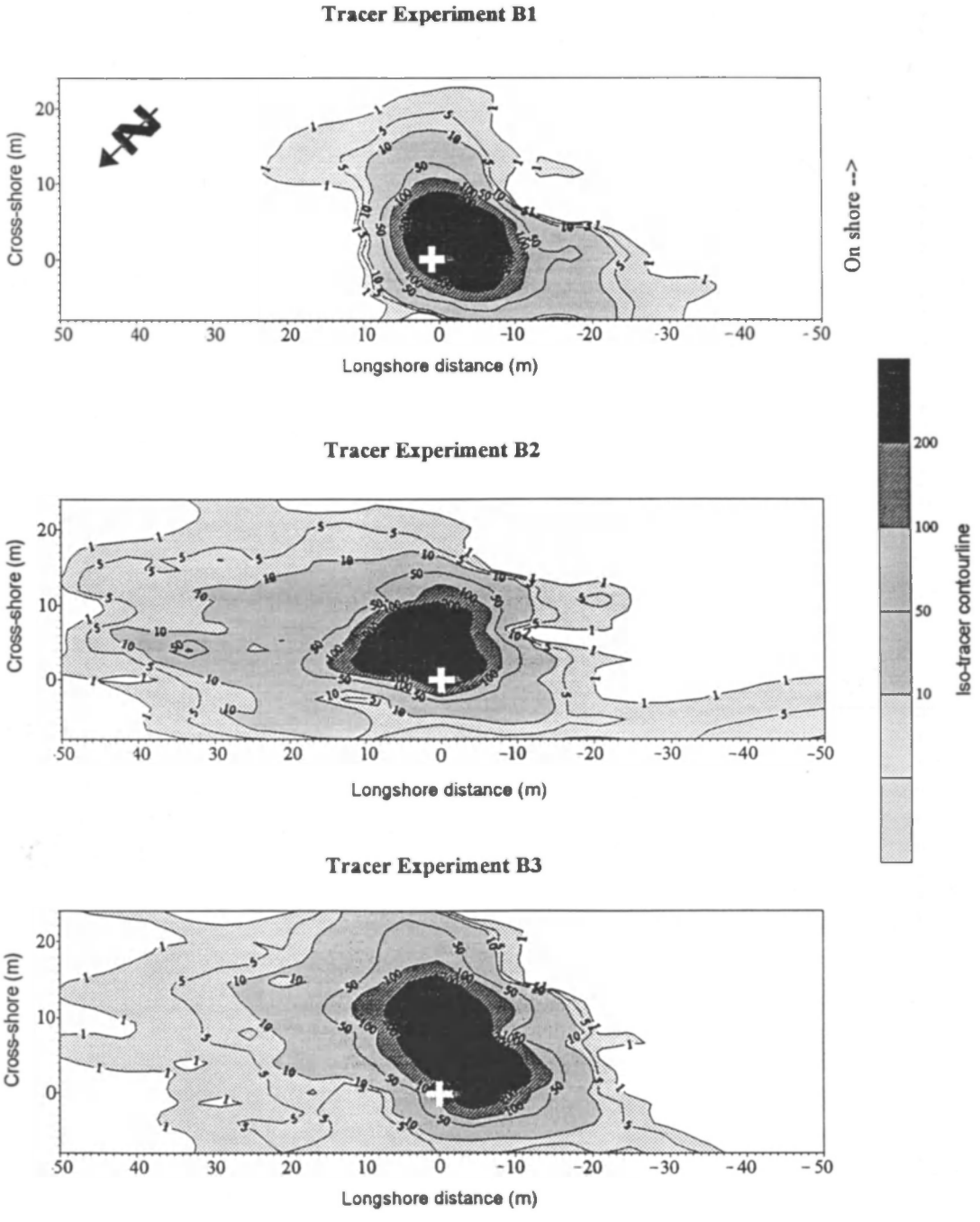

Figure 10. Iso-tracer contour map for the three detections carried out during tracer experiment B.

ginning (Julian day 51) and end of the experimental period (Julian day 63) have been superimposed (Figure 12a). The elevation difference between the profiles (Figure 12b) shows areas of local erosion and accretion.

Profile changes are most evident on the uppermost part of the profile, less than 150 m from the upper limit of the beach. The ridges on the high tidal zone moved shoreward during the 12 days between measurements. From the positive and negative elevation peak differences (Figure 12b), the average rates of onshore movement of the crests of the three upper shoreface ridges were estimated between 0.6 and 1.2 m per tidal cycle. This net movement (integrated over 24 tidal cycles) is assumed to be representative of the beach behavior during the tracer experiments (net beach motion integrated over 1 to 5 tidal cycles), since the incident wave climate remained consistently mild throughout the study period.

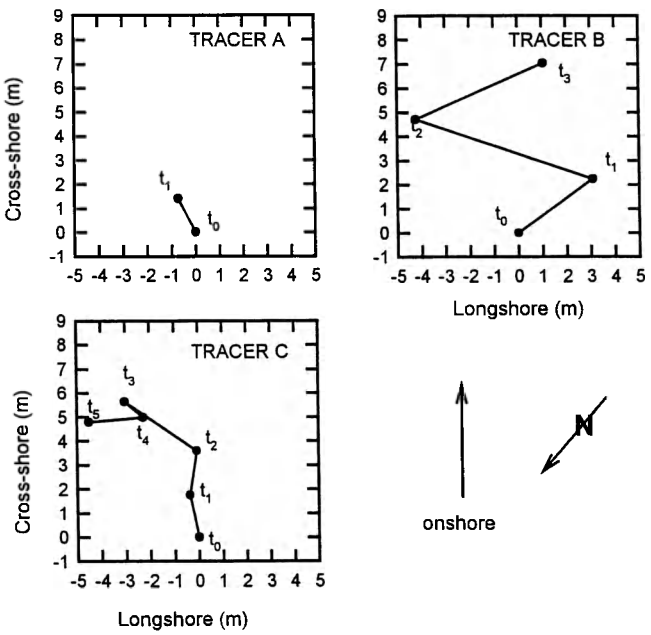

Figure 11. Tracer mass-centroid movement for the three tracing experiments (A, B and C) undertaken over the experiment period.

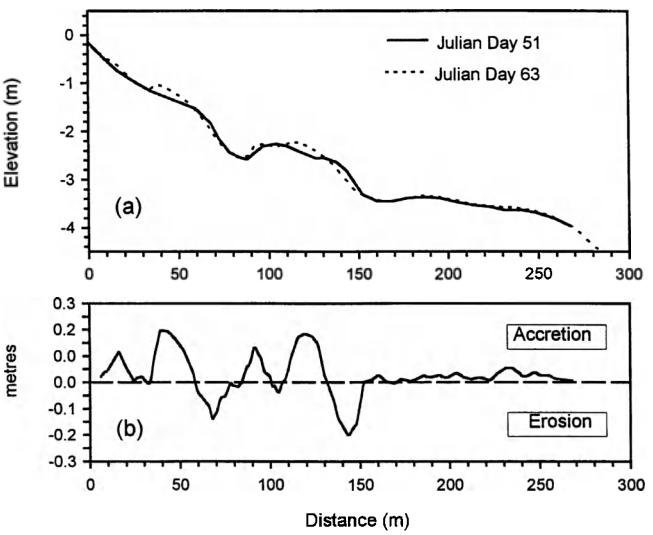

Figure 12. (a) Cross-sectional profiles of the high tide and mid tide intertidal zones (see Figure 4) taken on Julian day 51 (solid line) and 63 (dashed line), respectively. (b) Beach mobility across the high and mid intertidal zones expressed in terms of local sand elevation. Positive and negative changes indicate accretion and erosion, respectively over the study period.

A positive overall elevation difference for the uppermost part of the beach indicates a net spatially-averaged accretion of 2.9 cm. Accretion over the lower section is approximately 2 cm. This accretion/erosion imbalance along the cross-shore profile suggests the existence of longshore transport gradients or that the end of the profile at 270 m from the shoreline does not correspond to the closure depth of the profile.

To examine this imbalance, a three-dimensional analysis of the stability of the beach was undertaken using the data from all 11 transects (Figure 13). Accretional areas are shown as positive elevation differences (dark shading), while negative values (light shading) indicate erosional areas. Inferred movement of beach material is shown schematically on the figure by the two arrows (connecting areas of erosion with those of accretion). Cross-shore beach movement is onshore, while movement alongshore is towards the southwest (*i.e.*, France). The longshore beach movement is estimated to be of the order of 4 m per tidal cycle.

DISCUSSION

The ridges are subjected to hydrodynamic forces during the complete tidal cycle and for water depths ranging from a few millimeters to the full tidal range. However, the hydrodynamic data collected here, was limited to periods where instruments were fully submerged. The nature of the electromagnetic current meters (physical dimensions, installation procedures and principle of operation) require their installation to be some distance above the bed. This combined with the head of water required so that the sensor is not exposed during the passage of a wave trough limit the minimum water depth that data can be collected.

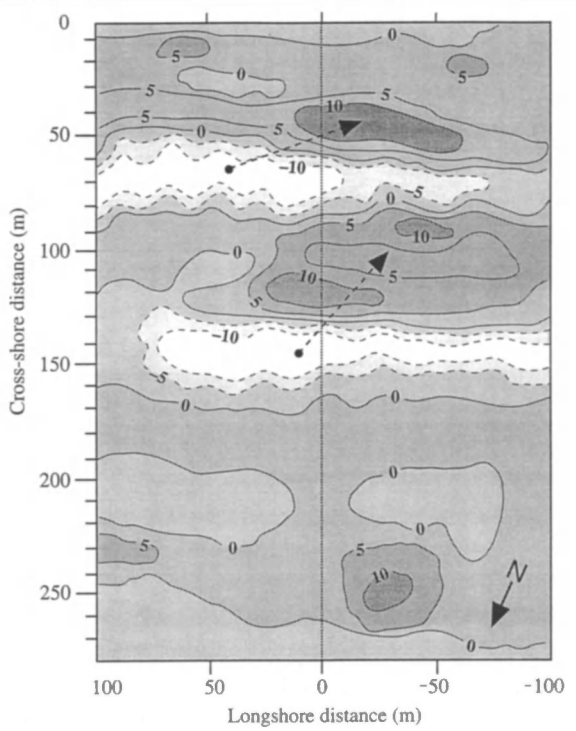

Figure 13. Contour map of changes in elevation of the high and mid intertidal zones over the experiment period (Julian day 51 to 63). This map was created from all transects shown on Figure 1. Positive and negative changes indicate accretion and erosion, respectively over the study period. Contour units in cm.

Table 2. *Immersed weight sediment transport rates (total) obtained from tracer experiments (see Table 1) and the application of Bailard's (1981) model.*

	Immersed Weight Sediment Transport Rate, I (kg/m/s² × 10^{-3})					
	Measured (tracer experiments)			Predicted (Bailard's model) (tracer experiments)		
Detection	I_y	I_x	$(I_y^2 + I_x^2)^{1/2}$	I_y	I_x	$(I_y^2 + I_x^2)^{1/2}$
A_1	31.2	60.6	66.6	3.5	72.5	72.6
B_1	−72.2	52.4	89.2	9.2	−2.2	9.5
B_2	117.0	40.8	125.0	22.8	−17.5	28.7
B_3	−67.3	29.7	73.6	20.9	−10.3	23.2
C_1	4.2	20.8	21.2	—	—	—
C_2	−3.9	25.5	25.8	—	—	—
C_3	34.9	24.1	42.4	—	—	—
C_4	−7.2	−6.2	9.7	77.8	59.0	97.6
C_5	37.0	−3.2	44.8	397.0	38.6	399.0

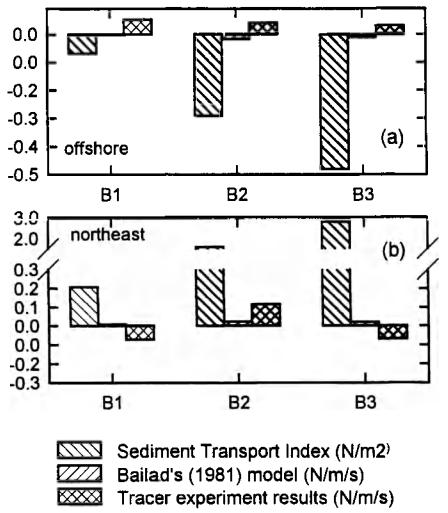

Figure 14. Comparison of tidal cycle averaged direction and relative magnitude of sediment transport during the tracer B experiment period. The data shown are the results of predictions using a deterministic sediment transport model approach (sediment transport index, see text); the energetic;'s approach (BAILARD, 1981) and the measured sediment transport rates during the tracer B experiment (see Table 2). (a) cross-shore direction (positive values indicate an onshore movement) and (b) longshore component (positive values indicate a northeasterly sediment movement).

Generally, sand transport pathways should be in agreement with the current patterns. Longshore currents flow towards the northeast, and dominate over the mean cross-shore current component. The latter consists of a steady, offshore flowing "undertow" component of approximately 5 cm/sec and a sea-surface driven component with an amplitude of about 5 cm/sec. In contrast, waves approaching from the west, contribute to northeasterly sand transport as shoaling creates an asymmetry in their profile. This interpretation of sand transport pathways, based on measured hydrodynamic conditions, is not consistent with directions obtained from the mass centroid movement during the tracer experiment (Figure 11). However, the tracer dispersion patterns (Figure 10) agree qualitatively with the hydrodynamic conditions. In particular there is a tendency for the tracer to be dispersed in response to wave direction and towards the northeast. The latter agreement implies that although sediment transport takes place during the period of hydrodynamic data collection, it does not consist of the dominant process which defines the net transport pattern as given by the centroid movement.

Quantitatively the transport rates obtained from the mass centroid analysis and the sediment transport models, respectively are shown in Table 2 and Figure 14. The tracer shows the cross-shore component of transport to be onshore, while the longshore component is towards the northeast only during B_2. For B_1 and B_3, transport is towards the southwest. On the other hand, both modelling approaches predict: (a) consistent offshore transport in cross-shore direction, (b) southeasterly transport in the longshore direction. Onshore sand transport was observed for the same beach under similar hydrodynamic conditions, during an early magnetic tracer experiment (VAN DER POST *et al.*, 1994). These observations suggest that the onshore migration of ridges is typical of the experimental area for the wave conditions experienced.

Assuming that ridge movement is analogous to ripple migration which is considered proportional to bedload transport rate (HUNTLEY *et al.*, 1991), then the observed topographic changes are in general agreement with the tracer results *i.e.* onshore movement of the ridge system at an average rate of approximately 1 m per tidal cycle. This rate compares with 2.3 m per tidal cycle, as indicated by onshore movement of the tracer. The difference between the two rates may be attributed to intercomparison between the 12-day averaged (neap–spring) profile analysis and tracer results representative of localised conditions over three tidal cycles, near springs. Overall, the observed migration rates are much higher than those observed by MULRENNAN (1992) (maximum 10 m per month (0.16 cm per tidal cycle)). In the longshore direction, net centroid movement is 1.03 m towards the southwest; this is the same direction derived from the topographic survey results (at 4 m/tidal cycle). The latter value is in very good agreement with the centroid movement alongshore, for B_1 and B_3, of 3.07 and 5.28 m, respectively. Most of the observed sediment movement occurs in the high tidal zone, with net accretion in the mid- and high tidal zones.

Tidally-integrated transport rates depend upon the intensity of the transport processes, throughout the associated tidal cycle. The particular intertidal location at which the data were collected is inundated over 36% of the tidal cycle and of this, 55% of the inundation time is associated with shoaling wave conditions. The disagreement between the patterns inferred from sediment transport models and the topographic data sets and tracer experiments might be explained, therefore, by assuming that the processes for the remaining 45% of the period of inundation, where no hydrodynamic data exists, could be dominant in determining the net morphological evolution of the ridges. These periods are characterised by shallow water depths, implying the dominance of inner surf and swash zone processes which are characterised by in-

creased levels of suspended load and infragravity motions (BEACH and STERNBERG, 1988; BEACH and HOLMAN, 1993). This is further supported by the increased values of STI and sediment transport rates estimated using the energetics model at shallow water depths (*see* Figures 8 and 9). The above interpretation agrees with the original generic definition of KING and WILLIAMS (1949), that the ridges are swash bars. Also, the experimental site falls within the typical locations (ORFORD and WRIGHT, 1978) where such swash bars occur (*i.e.* large tidal range; wide foreshore of low gradient; and short fetch). The location of the data collection station and the tracer experiments was near the high-tidal zone where MASSELINK (1993) showed that swash and surf zone processes are the dominant ones.

In the alongshore, sediment transport inferred from the hydrodynamics is towards the northeast, while tracer experiments and morphodynamic analysis show southeast transport direction. This might be due to tidal flow reversal during the last stages of the ebb (Figure 5). Such a change in direction, coupled with higher sediment resuspension processes during the ebb (*cf.* DAVIDSON *et al.*, 1993), dominate the transport pattern identified for the experimental area. Further, longshore movement of tracer could have resulted from wave-induced lateral flow towards the drainage channel (according to the mechanism suggested by DABRIO and POLO (1981)).

CONCLUSIONS

Hydrodynamic, morphological and sediment mobility data have been collected from a macrotidal, ridge and runnel beach under mild wave conditions. The information derived from the investigations are:

(1) Flow measurements show the mean cross-shore near-bed flow to consist of a steady 'undertow' component and a tidal component. The latter has been found to be driven by the sea surface elevation. Longshore currents are asymmetrical, with a dominant northerly flood flow. The relative steady component flow reversal towards the southwest has been observed during the last stages of the ebb.

(2) The transport patterns derived from the prevailing hydrodynamics under shoaling wave conditions contradict those observed from beach mobility. Combination of these results with the time-scale covered by each method suggests that swash/surf zone processes control the onshore transport of the ridges over the high-tidal zone, in accordance with the generic definition of ridges (KING and WILLIAMS, 1949). Alongshore sediment movement opposes that inferred from asymmetry of the tidal currents. This pattern is the result of wave-induced lateral flow in response to surf/swash zone processes and asymmetry in the availability of sediment for transport during the tidal cycle.

(3) In macrotidal environments the intertidal zone undergoes a number of different processes (shoaling waves, surf zone and swash zone). Certain parts of the intertidal zone and in particular the high-tidal zone are dominated by swash zone processes. The available instrumentation fails to measure these processes due to the shallow water depths. Any attempts to quantify sand transport and morphological development should be accompanied by measurements in these very shallow depths. Alternatively, different sediment transport study methods based upon different time-integrations periods can be utilised to reveal transport processes occuring in the swash zone.

ACKNOWLEDGEMENTS

The authors acknowledge M.P. Wilkin and A. de Resseguier for their assistance during the field data collection. Dr. D.G. Aubrey and Dr. E. Uchupi are thanked for their critical comments. The present study was funded by the Commission of the European Community (Directorate General for Science, Research and Development) under Contract No. MAS2-CT92-0024-C (C-STAB). This manuscript was prepared while one of the authors (G Voulgaris) was supported by Woods Hole Oceanographic Institution with a post-doctoral research award funded by the Mellon Foundation.

LITERATURE CITED

ADMIRALTY TIDE TABLES, 1994. European Waters, Volume 1, 446p.

BAGNOLD, R.A., 1963. Beach and nearshore processes. Part 1. Mechanics of marine sedimentation. *In:* HILL, M.N. (ed.), *The Sea*, Vol. 3. New York: Wiley-Interscience, pp. 507–528.

BAILARD, J.A., 1981. An energetics total load sediment transport model for a plane sloping beach. *Journal of Geophysical Research*, 86, 10938–10954.

BEACH, R.A. AND HOLMAN, R.H. 1993. Swash zone sediment transport on a steep beach. *EOS Transactions* (AGU), 74, 340.

BEACH, R.A. AND STERNBERG, R.W., 1988. Suspended sand transport in the surf zone: Response to cross-shore infragravity motion. *Marine Geology*, 80, 61–79.

BOWEN, A.J., 1980. *Simple Models of Nearshore Sedimentation; Beach Profiles and Longshore Bars in the Coastline of Canada Ottawa:* Geological Survey of Canada, pp. 21–30.

BOWEN, A.J.; CHARTHAND, D.M.; DANIEL, P.E.; GLODOWSKI, C.W.; PIPER, D.J.W.; READSHAW, J.S.; THIBAULT, J., AND WILLIS, D.H., 1986. *Canadian Coastal Sediment Study: Final Report of the Steering Committee*. National Research Council of Canada.

CONLEY, D.C. AND INMAN, D.L., 1992. Field observations of the fluid-granualr boundary layer under near-breaking waves. *Journal of Geophysical Research*, 97(C6), 9631–9643.

DABRIO, C.J. AND POLO, M.D., 1981. Flow regime and bedforms in a ridge and runnel system, S.E. Spain. *Sedimentary Geology*, 28, 97–110.

DAVIDSON, M.A.; RUSSEL, P.E.; HUNTLEY, D.A.; HARDISTY, J., AND CRAMP, A., 1992. An overview of the British beach and nearshore dynamics (B-BAND) programme. *Proc. 23rd Conf. Coastal Eng.*, pp. 1987–2000.

DAVIDSON, M.A.; RUSSEL, P.E.; HUNTLEY, D.A., AND HARDISTY, J., 1993. Tidal asymmetry in suspended sand transport on a macrotidal intermediate beach. *Marine Geology*, 110, 333–353.

DE MOOR, G., 1991. The beach nourishment of Bredene-De Haan and its impact on the beach morphology and the coastal evolution of the Belgian coast east of Oostende. *Proc. IGU Symposium "Coastal Protection"* (Nantes, October 1991).

DOWNING, J.P.; STERNBERG, R.W., AND LISTER, C.R.B., 1981. New instrumentation for the investigation of sediment suspension processes in the shallow marine environment. *In:* NITTROUER, C.A. (ed.), Sedimentary Dynamics of Continental Shelves. *Marine Geology*, 42, 19–34.

EINSTEIN, H.A., 1972. A basic description of sediment transport on beaches. *In:* MEYER, R.E. (ed.), *Waves on Beaches and Resulting Sediment Transport*. New York: Academic 462p.

FREDSOE, J., 1984. Turbulent boundary layer in wave-current motion. *Journal of Hydraulic Engineering* (ASCE), 110, 1103–1120.

FOOTE, Y.M. AND HUNTLEY, D.A., 1994. Velocity moments on a mac-

ro-tidal intermediate beach. *Coastal Dynamics, 94 (ASCE)*, pp. 794–808.

GUZA, R.T. AND THORNTON, E.B., 1985. Velocity moments in the nearshore. *Journal of Waterway, Port Coastal and Ocean Engineering*, 111(2), 235–256.

GUZA, R.T. AND THORNTON, E.B., 1989. Measuring surf zone dynamics. *In*: SEYMOUR, R.J. (ed.), *Nearshore Sediment Transport*. New York: Plenum pp. 51–60.

HAYES, M.O., 1972. Forms of sediment accumulation in the beach zone. *In*: MAEYR, R.E., (ed.), *Waves on Beaches*. New York: Academic, pp. 297–356.

HINE, A.C., 1979. Mechanisms of berm development and resulting beach growth along a barrier spit complex. *Sedimentology*, 26, 333–351.

HORIKAWA, K., 1981. Coastal sediment processes. *Annual Review of Fluid Mechanics*, 13, 9–32.

HOWA, H.L. AND DE RESSEGUIER, A., 1994. Application of a fluorescent grain detector/counter for sand transport evaluation in the littoral zone. *Proc. OCEANS '94*, III, 254–257.

HUNTLEY, D.A. AND BOWEN, A.J., 1975. Field measurements of nearshore velocities. *Proc. 14th Conference Coastal Engineering*, pp. 538–557.

HUNTLEY, D.A.; AMOS, C.L.; WILLIAMS, J.J., AND HUMPHREY, J.D., 1991. Estimating bedload transport on continental shelves by observations of ripple migration—An assesment. *In*: SOULSBY R.L. and BETTESS, R.,(eds.), *EUROMECH 262—Sand Transport in Rivers, Estuaries and the Sea*. Rotterdam, Balkema: pp. 17–24.

INMAN, D.L. AND CHAMBERLAIN, T.K., 1959. Tracing beach sand movement with irradiated Quartz. *Journal of Geophysical Research*, 64, 41–47.

JAFFE, B.E.; STERNBERG, R.W., AND SALLENGER, A.H., 1984. The role of suspended sediment in shore-normal beach profile changes. *Proc. 19th Conf. Coastal Eng.*, pp. 1983–1996.

KING, C.A.M. AND WILLIAMS, W.E., 1949. The formation and movement of sand bars by wave action. *Geographical Journal*, 113, 70–85.

KRAUS, N.C. AND J. SMITH, 1994. SUPERTANK Laboratory Data Collection Project, Vol. I: Main text. *Technical Report CERC-94-3*.

LACKNEUS, J.; DE MOOR, G, AND STOLK, A. 1994. Environmental setting, morphology and volumetric evolution of the Middelkerke Bank (southern North Sea). *Marine Geology*, 121, 1–22.

MADSEN, O.S., 1991. Mechanics of cohesionless sediment transport in coastal waters. *Coastal Sediments' 91* (ASCE), pp. 15–27.

MADSEN, O.S. AND GRANT, W., 1976. Sediment transport in the coastal environment. Report No. 209. Ralph M. Parsons Laboratory, Dept. of Civil Engineering, MIT Cambridge, Massachusetts, 105p.

MASON, C.; BIRKEMEIER, W.A., AND HOWD, P.A., 1988. Overview of DUCK85 nearshore processes experiment. *Coastal Sediments '87* (ASCE), pp. 818–833.

MASSELINK, G., 1993. Simulating the effects of tides on beach morphodynamics. *Journal of Coastal Research*, 15, 180–97.

MEYER-PETER, E. AND MULLER, R., 1948. Formulas for bed-load transport. *Proc. 2nd Congress IAHR* (Sweden), 2, 39–64.

MULRENNAN, M.E., 1992. Ridge and runnel beach morphodynamics: An example from the central east coast of Ireland. *Journal of Coastal Research* 8(4), 906–918.

NIELSEN, P., 1984. Measurements of time-averaged suspended sediment concentrations under waves. *Coastal Engineering*, 8, 51–72.

ORFORD, J.D. AND WRIGHT, P., 1978. What's in a name?—Descriptive or genetic implications of ridge and runnel' topography. *Marine Geology*, 28, M1–M8.

OWENS, E.H. AND FROBEL, D.H., 1977. Ridge and runnel systems in the Magdalen Islands, Quebec. *Journal of Sedimentary Petrology*, 47, 191–198.

ROELVIK, J.A. AND STIVE, M.J.F., 1989. Bar-generating cross-shore flow mechanisms on a beach. *Journal of Geophysical Research*, 94, 4785–4800.

ROSATI, J.D.; GINGERICH, K.J., AND KRAUS, N.C, 1990. SUPERDUCK Surf Zone Sand Transport Experiment. *Technical Report—CERC*, pp. 51.

SCHOONES, J.S. AND THERON, A.K., 1995. Evaluation of 10 cross-shore sediment transport/morphological models. *Coastal Engineering*, 25, 1–41.

SCOTT, K.A.; THORTON, E.B., AND BIRKEMEIER, W., 1991. Mean currents and sediment transport at DELILAH. *Coastal Sediments '91* (ASCE), pp. 477–488.

SIMMONDS, D.; VOULGARIS, G., AND HUNTLEY, D.A., 1995. Dynamic processes on a ridge and runnel beach. *Coastal Dynamics 95* (ASCE, Gdansk, Poland), pp. 868–878.

SOULSBY, R.L.; HAMM, L.; KLOPMAN, G.; MYRHAUG, D.; SIMMONS, R.R., AND THOMAS, G.P., 1993. Wave-current interaction within and outside the bottom boundary layer. *Coastal Engineering*, 21, 41–69.

STERNBERG, R.W.; SHI, N.C. AND DOWNING, J.P., 1989. Continuous measurements of suspended sediment. *In:* SEYMOUR, R.J. (ed.), *Nearshore Sediment Transport Study*. New York: Plenum pp. 231–57.

VAN DER POST, K.D.; OLDFIELD, F., AND VOULGARIS, G., 1994. Magnetic tracing of beach sand: Preliminary Results. *Coastal Dynamics '94* (ASCE), pp. 323–334.

VINCENT, C.E.; HANES, D., AND BOWEN, A.J., 1991. Acoustic measurements of suspended sand on the shoreface and the control of conentration by bed roughness. *Marine Geology*, 96, 1–18.

VOULGARIS, G., 1996. Bailard Modelling. *In:* O'CONNOR, B.A. (ed.), *Circulation and Sediment Transport Around Banks (CSTAB) Handbook*: Department of Civil Engineering, University of Liverpool: pp. 192–201.

VOULGARIS, G. AND COLLINS, M.B., 1996. Suspended Sediment Fluxes. *In:* O'CONNOR, B.A., (ed.), *Circulation and Sediment Transport Around Banks (CSTAB) Handbook*. Liverpool: Department of Civil Engineering, University of Liverpool, pp. 495–547.

WHITE, T.E., 1987. Nearshore Sand Transport. Unpublished Ph.D. Thesis. University of California, San Diego. 210p.

WRIGHT, L.D. AND SHORT, A.D., 1984. Morphodynamics variability of surf zones and beaches. A synthesis. *Marine Geology*, 5, 93–116.

WRIGHT, L.D.; NIELSEN, P.; SHORT, A.D., AND GREEN, M.O., 1982. Morphodynamics of a macrotidal beach. *Marine Geology*, 50, 97–128.

YALIN, M.S., 1977. *Mechanics of Sediment Transport* Oxford: Pergamon 290p.